ISTITUTO NAZIONALE DI FISICA NUCLEARE
Laboratori Nazionali di Frascati

LNF-76/66

G. Bologna, V. Bellini, V. Emma, A. S. Figuera, S. Lo Nigro, C. Milone and G. S. Pappalardo: FISSION OF Bi, Pb, Au AND Pt INDUCED BY A COHERENT PHOTON BEAM FROM 1000 MeV EOECTRONS.

Nuovo Cimento 35A, 91 (1976)

Servizio Documentazione
dei Laboratori Nazionali di Frascati
Cas. Postale 13 - Frascati (Roma)

IL NUOVO CIMENTO Vol. 35 A, N. 1 1 Settembre 1976

Fission of Bi, Pb, Au and Pt Induced by a Coherent Photon Beam from 1000 MeV Electrons (*).

G. Bologna

Laboratori Nazionali del CNEN - Frascati, Italia

V. Bellini, V. Emma, A. S. Figuera, S. Lo Nigro, C. Milone and G. S. Pappalardo

Istituto di Fisica Generale dell'Università - Catania
Istituto Nazionale di Fisica Nucleare - Sezione di Catania

(ricevuto il 14 Giugno 1976)

Summary. – The photofission yields of Bi, Pb, Au and Pt induced by a coherent bremsstrahlung beam from 1000 MeV electrons striking a diamond single crystal have been measured. The experiment has been performed at sixteen different energies of the main peak of the photon spectrum, in the energy range between 220 MeV and 500 MeV, by detecting the fission fragments with glass sandwiches. All the photon spectra have been measured simultaneously to the exposures of the fissionable samples by means of a magnetic pair spectrometer and a real-time acquisition system with an on-line computer. An appropriate unfolding method was developed in order to deduce the behaviour of the photofission cross-section from the experimental yields. The estimated cross-section curves clearly show a first resonance at a photon energy of about 320 MeV with a FWHM $\approx$ 125 MeV, whilst there is only a hint of a second broad resonance centred at $k \approx 750$ MeV. The very good agreement between the position of the first resonance put in evidence in the present experiment and the energy of the first baryon resonance in the pion photoproduction is attributed to a predominance of the photomesonic mechanism in the photofission process of the investigated elements.

(*) This work has been partially supported by CRRN and CSFNeSM.

1. – Introduction.

The interaction between photons with energy $k \geqslant 140$ MeV and heavy nuclei has been largely studied ([1-17]) with the aim to deduce some information on the excitation and the subsequent de-excitation mechanism through the fission channel at energies at which pion photoproduction from single nucleons is possible. This information can be drawn out from the analysis of the cross-section behaviour *vs.* the photon energy.

Until now, for $k \geqslant 140$ MeV energies, bremsstrahlung beams from an amorphous target have been used as photon sources and the quantity experimentally deduced is the photofission yield per equivalent quantum $g(k_{\max})$ for a number of the maximum energies of the bremsstrahlung spectrum. Among the different methods used to deduce the fission cross-section $f(k)$ from the experimental yields, the « photon difference » method ([18]) has been largely employed.

Recently the problem has been faced by directly solving the Volterra linear equation in the form

$$g(k_{\max}) = \int_0^{k_{\max}} \mathcal{N}(k, k_{\max}) f(k)\, \mathrm{d}k \,, \tag{1}$$

([1]) G. BERNARDINI, R. REITZ and E. SEGRÈ: *Phys. Rev.*, **90**, 573 (1953).
([2]) J. A. JUNGERMAN and H. M. STEINER: *Phys. Rev.*, **106**, 585 (1957).
([3]) E. V. MINARIK and V. A. NOVIKOV: *Sov. Phys. JETP*, **5**, 253 (1957).
([4]) H. G. DE CARVALHO, A. CELANO, G. CORTINI, R. RINZIVILLO and G. GHIGO: *Nuovo Cimento*, **19**, 187 (1961).
([5]) H. G. DE CARVALHO, G. CORTINI, D. DEL GIUDICE, G. POTENZA, R. RINZIVILLO and G. GHIGO: *Nuovo Cimento*, **32**, 1717 (1964).
([6]) F. CARBONARA, H. G. DE CARVALHO, R. RINZIVILLO, E. SASSI and G. P. MURTAS: *Nucl. Phys.*, **73**, 385 (1965).
([7]) YU. N. RANYUK and P. V. SOROKIN: *Sov. Journ. Nucl. Phys.*, **5**, 26 (1967).
([8]) A. V. MITROFANOVA, YU. N. RANYUK and P. V. SOROKIN: *Sov. Journ. Nucl. Phys.*, **6**, 512 (1968).
([9]) L. G. MORETTO, R. C. GATTI, S. G. THOMPSON, J. T. ROUTTI, J. H. HESENBERG, L. M. MIDDLEMAN, M. R. YEARIAN and R. F. HOFSTADTER: *Phys. Rev.*, **179**, 1176 (1969).
([10]) T. METHASIRI: *Nucl. Phys.*, **158** A, 433 (1970).
([11]) V. EMMA, S. LO NIGRO and C. MILONE: *Lett. Nuovo Cimento*, **2**, 117, 271 (1971).
([12]) T. METHASIRI and S. A. E. JOHANSSON: *Nucl. Phys.*, **167** A, 97 (1971).
([13]) Y. WAKUTA: *Journ. Phys. Soc. Jap.*, **31**, 12 (1971).
([14]) G. A. VARTAPETYAN, N. A. DEMEKHINA, V. I. KASILOV, YU. N. RANYUK, P. V. SOROKIN and A. G. KHUDAVERDYAN: *Sov. Journ. Nucl. Phys.*, **14**, 37 (1972).
([15]) G. ANDERSSON, I. BLOMQVIST, B. FORKMAN, G. G. JONSSON, A. JÄRUND, I. KROON, K. LINDGREN and B. SCHRØDER: *Nucl. Phys.*, **197** A, 44 (1972).
([16]) P. DAVID, J. DEBRUS, U. KIN, G. KUMBARTZKI, H. MOMMSEN, W. SOYEZ, K. H. SPEIDEL and G. STEIN: *Nucl. Phys.*, **197** A, 163 (1972).
([17]) G. BOLOGNA, V. EMMA, A. S. FIGUERA, S. LO NIGRO and C. MILONE: *Phys. Lett.*, **52** B, 192 (1974).
([18]) L. KATZ and A. G. W. CAMERON: *Can. Journ. Phys.*, **29**, 518 (1951).

where $\mathcal{N}(k, k_{max})$ is the number of photons per unit k interval, when the maximum photon energy is k_{max}. The $f(k)$ behaviours deduced by different analytical methods ([2,3,5,6,8-16]) show some discrepancies that do not permit to give an obvious interpretation of the photofission mechanism, especially in the region where mesonic effects can be expected, due to the formation of the first baryon excited state.

Considerable difficulties are found in solving the equation of the type (1), as it is well known ([18-28]) that it is particularly unstable. In the case of measurements made with bremsstrahlung beam from an amorphous target the situation is very critical, since the kernel $\mathcal{N}(k, k_{max})$ has a very weak dependence on the energy ([20]).

To deduce with good reliability the behaviour of $f(k)$, a sensible improvement over bremsstrahlung beam from an amorphous target can be obtained by using a coherent bremsstrahlung beam, as shown by our preliminary results ([17]). This coherent photon beam is characterized by a « quasi-monoenergetic » main peak lying on a continuous spectrum ([29-31]).

In the present experiment we used the coherent bremsstrahlung beam produced by 1000 MeV electrons striking a diamond single crystal, in order to study the fission in Bi, Pb, Au and Pt. The measurements have been performed by changing the energy of the main photon peak in the range from 200 MeV to 500 MeV, as we were mainly interested in the investigation of photomesonic effects in the fission process. For this purpose, the possible resonant behaviour of the cross-section is relevant. Thus, absolute values are not required and we used only very thick targets.

We did not consider nuclides with $Z \geqslant 83$, in order to avoid difficulties arising from dipole absorption of photons (giant resonance), which can obscure the mesonic effects we want to study.

([19]) A. S. PENFOLD and J. E. LEISS: *Phys. Rev.*, **114**, 1332 (1959).
([20]) D. L. PHILLIPS: *Journ. Assoc. Comput. Mach.*, **9**, 84 (1962).
([21]) S. TWOMEY: *Journ. Assoc. Comput. Mach.*, **10**, 97 (1963).
([22]) B. C. COOK: *Nucl. Instr.*, **24**, 256 (1963).
([23]) J. T. ROUTTI: UCRL-18514, Lawrence Rad. Lab. (Berkeley, Cal., 1969).
([24]) K. TESCH: *Nucl. Instr.*, **95**, 245 (1971).
([25]) V. F. TURCHIN, V. P. KOZLOV and M. S. MALKEVICH: *Sov. Phys. Usp*, **13**, 681 (1971).
([26]) E. BRAMANIS, T. K. DEAGUE, R. S. HICKS, R. J. HUGHES, E. G. MUIRHEAD, R. H. SAMBEL and R. J. J. STEWART: *Nucl. Instr.*, **100**, 59 (1972).
([27]) C. YAMAGUCHI, T. SHINTOMI and M. MASUDA: *Nucl. Instr.*, **106**, 471 (1973).
([28]) V. F. TURCHIN and L. S. TUROVCEVA: *Sov. Math. Dokl.*, **14**, 1430 (1973).
([29]) G. BOLOGNA, G. DIAMBRINI and G. P. MURTAS: *Phys. Rev. Lett.*, **4**, 572 (1960).
([30]) G. BARBIELLINI, G. BOLOGNA, G. DIAMBRINI and G. P. MURTAS: *Phys. Rev. Lett.*, **8**, 454 (1962); *Nuovo Cimento*, **28**, 435 (1963).
([31]) G. BOLOGNA: *Nuovo Cimento*, **49** A, 756 (1967).

When one uses a coherent photon beam, the equation describing the process is a linear Fredholm equation of the first kind (see sect. 4), different from eq. (1) in the upper limit of the integral, which is fixed at 1000 MeV (photon maximum energy) with the kernel properly modified for the shape of the photon spectrum used in the experiment.

The experimental yields, for $k_{max} = \text{constant}$, depend noticeably on the energy of the first main peak that characterizes the photon spectrum.

For solving the integral equation of the process we used a partially new unfolding method ([32]), which, once applied to our experimental data, permitted to deduce the behaviour of the photofission cross-section in a more reliable way than the conventional methods.

2. – Experimental procedure.

2·1. *Coherent photon beam.* – The photon beam obtained at the Frascati electronsynchrotron by 1000 MeV electrons striking a diamond single crystal has a main peak at energy k_j with a few secondary peaks at higher energies,

TABLE I. – *Standard deviation S_d of the least-square fit for each photon spectrum vs. the k_j energy of the main peak.* The standard deviation for each k_j value is ± 0.5 MeV.

k_j (MeV)	S_d
223	1.39
246	1.11
253	1.11
263	1.01
284	1.30
292	1.10
318	1.23
334	1.05
353	1.36
379	1.01
398	1.26
419	1.12
428	0.97
449	1.18
467	1.08
491	1.19

([32]) G. BOLOGNA and G. S. PAPPALARDO: to be published.

but smaller in amplitude. k_j is approximately the energy of the mean point at the decreasing slope; for details on the exact definition see ref. ([29-31]).

The energy k_j depends on the angle between the direction of a crystal axis of the diamond crystal and the electron beam. Then, by using sixteen orientations with respect to the electron beam, at $E_0 = 1000$ MeV fixed energy, we obtained sixteen different photon spectra, in which the energy k_j of the main peak ranged from 220 MeV to 500 MeV (see table I).

As the position of the peaks in the spectrum depends critically on the crystal orientation, each spectrum had to be separately measured. The experimental equipment used to measure the spectrum concurrently with the irradiation of the photofission samples is sketched in fig. 1.

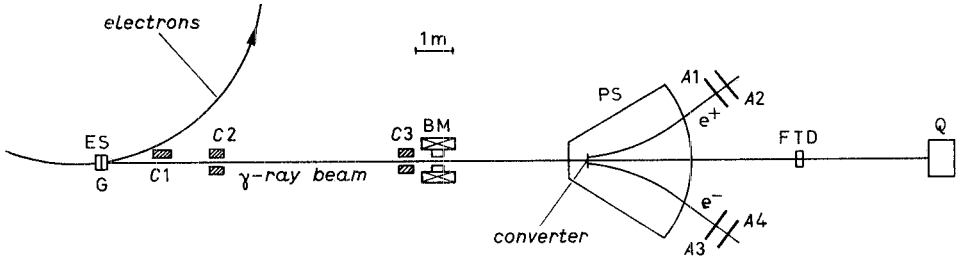

Fig. 1. – Experimental arrangement. ES, electronsynchrotron; G, goniometer with the diamond radiator; $C1$, scraper; $C2$ and $C3$, lead collimators; BM, broom magnet; PS, magnetic pair spectrometer; $A1$, $A2$, $A3$ and $A4$, scintillation telescopes; FTD fission target and detector apparatus; Q, quantameter.

ES represents the 1 GeV electronsynchrotron, G the goniometer on which the diamond radiator is mounted. This one has the shape of a flat plate 2 mm thick (equal to about 0.02 r.l.) with the face (10×5) mm^2 cut normal to the [110]-axis. The crystal can rotate around two axes normal to each other, in such a way that the angle between the [110]-axis and the direction of the electron beam can be changed. For our purposes the maximum value of this angle is 60 mrad, and the sensitivity of the goniometer is 0.1 mrad.

The coherent photon beam coming from the diamond firstly meets a scraper $C1$, which is as near as possible to the radiator. This scraper limits the effect of the multiple traversal of the electrons in the source. Next, the beam passes through two circular collimators $C2$ and $C3$. The last one defines the beam size with an angular acceptance of 1 mrad. The $C2$ collimator has a little larger acceptance. Its function is only to limit the generation of the electromagnetic showers in $C3$. BM is a broom magnet and PS is a magnetic pair spectrometer, described in ref. ([33]) and used to measure the energy spectrum

([33]) G. BOLOGNA, G. DIAMBRINI, R. TOSCHI, A. S. FIGUERA, U. PELLEGRINI, B. RISPOLI and A. SERRA: *Nucl. Instr.*, **12**, 263 (1961).

of the photon beam. The aluminum converter is 10^{-4} r.l. thick. The e^+e^- pairs, bent by the magnetic field of the spectrometer, are detected by two scintillation counter telescopes ($A1$, $A2$) and ($A3$, $A4$), placed symmetrically with respect to the photon beam. The momentum acceptance of these two telescopes is $\Delta p/p = 4\,\%$. The γ-ray beam emerging from the spectrometer firstly crosses the FTD apparatus (fission target and detector), that will be described in subsect. 2·2, and finally stops in a Wilson quantameter used as a monitor. The total thickness crossed by the beam in FTD is about 0.1 r.l. and remains constant in all the exposures.

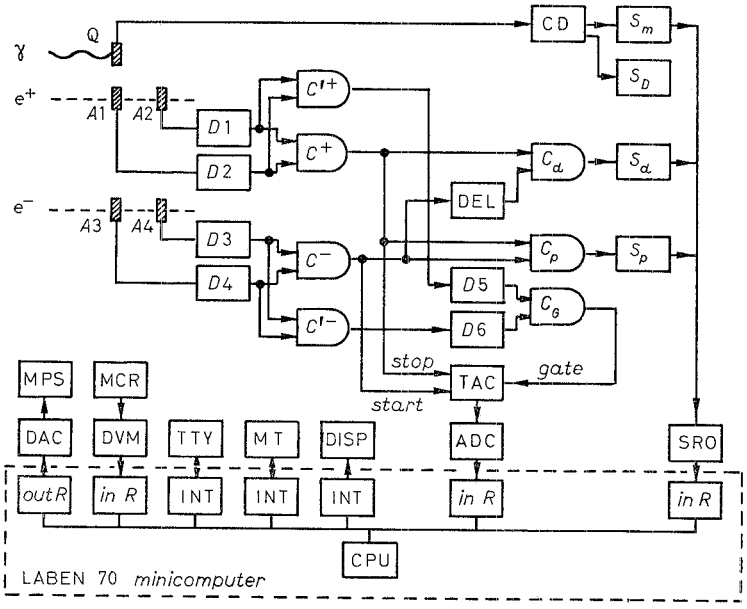

Fig. 2. – Block diagram of the electronic detection apparatus and the real-time data acquisition system used to measure on-line the photon energy spectrum.

Figure 2 shows the electronic detection apparatus and the real-time data acquisition system used to measure on-line the photon energy spectrum.

The signals coming from $A1$, $A2$, $A3$ and $A4$ are shaped by the discriminators $D1$, $D2$, $D3$ and $D4$ We have first a double-coincidence system $C^+ = A1 \cdot A2$ and $C^- = A3 \cdot A4$. Thereafter we have a system of prompt coincidences $C_p = C^+ \cdot C^-$ and of delayed coincidences $C_d = C^+ \cdot (C^-$ delayed). The delay (DEL) on C^- is 23 ns, which is the time separation between two successive electron bunches in the electronsynchrotron. In such a way we separately measure the prompt and delayed coincidences. These are recorded by the scalers S_p and S_d, respectively. The scalers S_m and S_D record the pulses coming from a charge digitizer (CD) connected with the quantameter Q. The

scaler S_D is manually reset each time the photofission samples are changed, and gives the exposure dose.

The scalers S_p, S_d and S_m are connected with a read-out module (SRO). As the resolution time of the coincidences C_p and C_d is 8 ns, the described counting method is adequate as long as the intensity of the γ-ray beam is less than $\approx 10^8$ equivalent quanta/s. In this case the accidental coincidences are about 10 % of the true ones.

In order to obtain an accurate measurement even in the case of more intense photon beams, we developed the following system, which reduces the resolution time to $\pm$ 0.5 ns, as we will see below. The outputs of the coincidences C^- and C^+ are sent, after suitable delays (not reported in fig. 2), to the start or, respectively, the stop inputs of a time-to-amplitude converter (TAC), which measures the time-of-flight (TOF) spectrum between e^+ and e^-, that is the distribution of the delay of arrival between e^+ and e^-. In order to eliminate the pulse pile-up at the input, the TAC is gated by the coincidence C_G, obtained in turn from the coincidences C'^+ and C'^-. The discriminators $D5$ and $D6$ send long-shaped pulses to C_G, in order to increase the resolution time to a required value of 100 ns.

The TAC output is connected with a 1024-channel analog-to-digital converter (ADC).

The electronic apparatus is completed by a digital voltmeter (DVM) and by a digital-to-analog converter (DAC), that controls the magnet power supply (MPS). The DVM measures the voltage across a calibrated resistor (MCR) placed in series with the coils of the magnet and gives the energy of the photons by a proper calibration.

The read-out system of the scalers, the ADC and the DVM are interfaced to the central processing unit (CPU) of the LABEN 70 minicomputer by three standard input channels (or registers), whereas the DAC is interfaced by a standard output channel. This real-time digital acquisition system has 8 K words of 16 bit core storage and is completed by a teletype (TTY), by a 9-track magnetic-tape unit (MT) and by a point display unit (DISP).

The operation of all these peripheral devices is overlapped on a priority basis, the priorities being hardware assigned in decreasing order as follows: MT, ADC, SRO, DVM, DAC, TTY, DISP.

The operation of the system is started by setting on the TTY keyboard the initial and the final energies and the increment relevant to the bremsstrahlung spectrum to be measured. From now on, the spectrum measurement proceeds automatically, except for manual intervention by the operator in case of unexpected contingency.

The required energy is constantly compared with the actual energy measured by the DVM about twice a second; if necessary, the system operates the correction via the DAC. The correction rate depends on the amount of the correction itself, in such a way that oscillations, which could be triggered

in the loop, are damped. The stop signal is produced when the scaler S_m reaches a preset counting. At the same time the bremsstrahlung spectrum or, alternatively, the time-of-flight spectrum can be stored in the minicomputer memory and presented on the display unit, as shown in fig. 3*a*) and *b*), respectively.

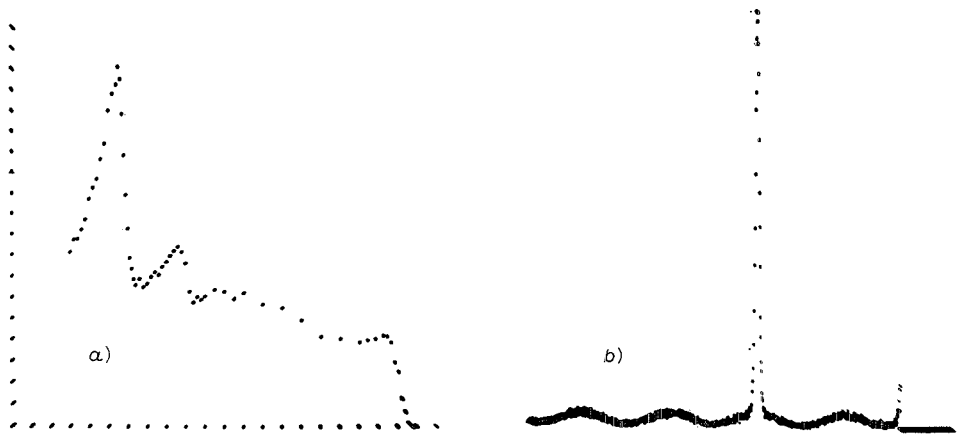

Fig. 3. – *a*) Bremsstrahlung spectrum and *b*) time-of-flight spectrum as observed on the minicomputer display unit.

The TOF spectrum shown in fig. 3*b*) consists of a narrow spike, corresponding to the true coincidences, which is superimposed to a background of accidental events. The conversion range of the TAC has been fixed to 100 ns; thus, four different regions can be singled out, which correspond to four electron-synchrotron bunches, each of 23 ns duration.

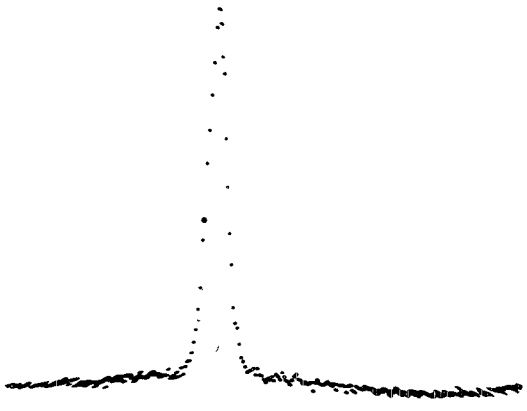

Fig. 4. – Partial representation of the time-of-flight spectrum of fig. 3 *b*) on enlarged scale base.

Figure 4 is a partial representation of fig. 3*b*) on enlarged scale base. By counting the channels contained in the width at half maximum of the spike it can be easily seen that, with 1024 channels distributed over 100 ns, the resolution time of this kind of apparatus is $\pm$ 0.5 ns.

After the stop signal, all the data processing is done in a total time of less than 10 ms (the minicomputer cycle is 1.3 μs). In practice, the difference $S_p - S_d$, which gives the number of true coincidences, is performed. Furthermore all channels of the TOF spectrum included in the spike bunch of fig. 3*b*) are added; from this result the sum of the other three bunches divided by three is subtracted. This method allows an on-line precise measurement of the bremsstrahlung spectrum, even when the γ-ray beam intensity is larger than 10^8 equivalent quanta/s.

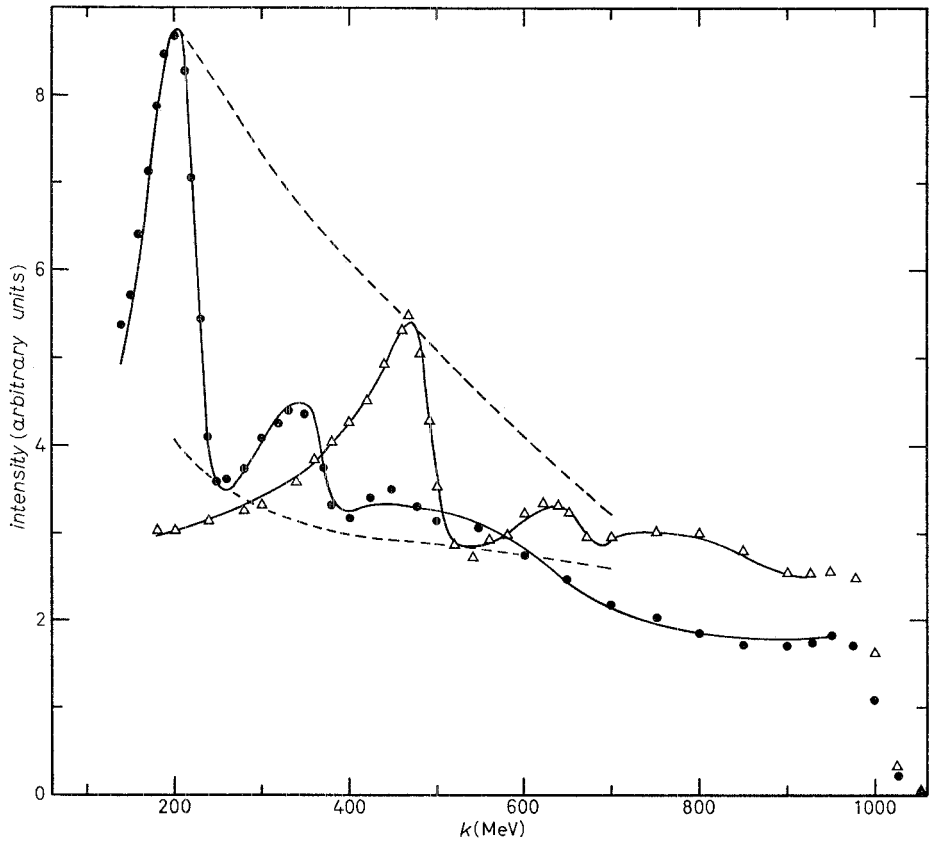

Fig. 5. – Coherent bremsstrahlung intensity of $E_0 = 1000$ MeV electrons in a diamond crystal *vs.* the photon energy k. The dots and the triangles represent the measured intensities in the spectra having the main peak at $k_j = 223$ MeV and $k_j = 491$ MeV, respectively. The solid curves are the least-square fits, the dashed ones show where the maximum and the minimum of the main peak lie as the crystal orientation is changed.

The content of the TOF spectrum, as well as all the other data relevant for the measurement, is then recorded on a magnetic tape to make a subsequent more refined off-line processing possible, if required (by making, for instance, a least-square fit of the TOF spectrum with suitable functions). Obviously, only the essential data are also printed on the TTY.

At this time the scalers and the memory region reserved for the TOF spectrum are reset, the energy is incremented and the already-described operation cycle is automatically started for a new point of the bremsstrahlung spectrum, until the final energy is reached.

Two typical experimental photon spectra for different orientations of the diamond crystal are shown in fig. 5. The dots and the triangles represent the bremsstrahlung intensities $kn(k, k_j)$ measured as a function of the photon energy k, $n(k, k_j)\,\mathrm{d}k$ being the number of photons with energy between k and $k + \mathrm{d}k$. The sizes of the symbols are of the same order of magnitude of the statistical errors ($\leqslant 2\,\%$). The solid curves represent the least-square fits. Experimental effects like electron multiple scattering in the crystal, divergence of the circulating electron beam, collimation of the photon beam, energy resolution of the pair spectrometer are all taken into account for the calculation of the spectra.

The standard deviation of the least-square fit for each spectrum is given in table I as a function of the energy k_j. The corresponding standard deviation for all k_j values is $\Delta k_j \approx \pm 0.5$ MeV. In fig. 5 we give also two dashed curves that show where the maximum and the minimum of the main peak lie when the crystal orientation is changed. These curves clearly show that the amplitude of the first main peak decreases when k_j advances toward the electron energy E_0. In fact, the ratio R of the values of the first maximum to the first minimum in the photon spectrum is a function of E_0 and k_j as given by

$$R \propto \frac{E_0}{k_j}(E_0 - k_j)\,. \tag{2}$$

For this reason we made measurements only for $k_j < 500$ MeV and kept constant the electron energy E_0 at the maximum available energy of the Frascati electronsynchrotron. The spectra of fig. 5 correspond to the maximum (491 MeV) and minimum (223 MeV) k_j value used in our experiment.

The photon density per monitor unit, *i.e.* per equivalent quantum, except for a constant, is given by

$$\mathcal{N}(k, k_j) = \frac{n(k, k_j)}{\int_0^{E_0} kn(k, k_j)\,\mathrm{d}k}\,. \tag{3}$$

For experimental reasons it was not possible to measure the photon spectra for $k < 150$ MeV. Thus in eq. (3) we used the result of the least-square fit,

which gives a sufficiently high confidence level. This was obtained at the price of a high statistical accuracy and of a refined measurement method.

2·2. *Fission fragment detection.* – The fission fragments have been detected by means of the glass sandwich technique, that we previously described ([11,34]).

We used metal targets (25×25) mm^2 of surface and 0.2 mm thick, each sandwiched between two glass plates. The photon beam was orthogonal to the glass sandwiches and had a cross-sectional diameter of about 2 cm, as tested by Polaroid plates.

At each k_j value of the photon spectrum we irradiated firstly two sandwiches containing, in the order, Bi and Pb samples at a dose of 10^{12} equivalent quanta and successively two sandwiches containing Au and Pt at a dose of $3 \cdot 10^{12}$ equivalent quanta; the corresponding irradiation time was about 1.5 h and 4 h, respectively. This alternative exposure at the same k_j was done in order to reduce the photon spectrum distortions which take place in crossing each sandwich.

After exposure, the glass plates were etched with a 4% HF solution for 25 min at 25 °C. The fission tracks have been observed by an optical microscope connected with a telecamera and a video display (*) with a total magnification of 400×. This scanning system gives a good accuracy in the discrimination of the fission tracks from the damage of the glass plates, due to the large irradiation intensity.

The stability of the criteria of track selection was checked by periodically scanning some plates selected at random. In fifty different scannings of the same glass surface we counted a number of fission tracks nearly constant with a maximum deviation of $\pm 2\%$ from the average value.

For the same glass plates we also scanned different surfaces of equal area, contiguous to each other and symmetrical with respect to the photon beam. In this way the sampling error was estimated and it was, on the average, less than 3% for all the plates. All the glass plates were scanned independently by two scanners and the results agreed within the statistical errors.

By entirely scanning the irradiated surface of some plates we have tested the centre and the actual cross-sectional area of the photon beam on the plates; we observed that the fission events had a distribution which can be very nearly approximated by a bivariate Gaussian distribution centred on the photon beam, of which it reproduce the space distribution.

Taking into account these results, for all the other plates we have scanned only two rectangular strips (25×1.25) mm^2 of area, orthogonal to each other and centred with respect to the photon beam. For each sandwich we scanned both the plates that detected the fragments emitted forward and backward

---

([34]) V. EMMA, S. LO NIGRO and C. MILONE: *Nucl. Phys.*, **257** A, 438 (1976).

(*) MICROVIDEOMAT system made by C. Zeiss, Oberkochen, West Germany.

with respect to the direction of the photon beam. As the target thickness is very large with respect to the average range of fission fragments, we observe only one of the binary-fission tracks.

A total of about $1.5 \cdot 10^6$ tracks was collected.

3. – Experimental results.

We deduced the photofission yields $g(k_j)$ from the numbers of fission tracks counted in the scanned surfaces, taking into account the exposure dose

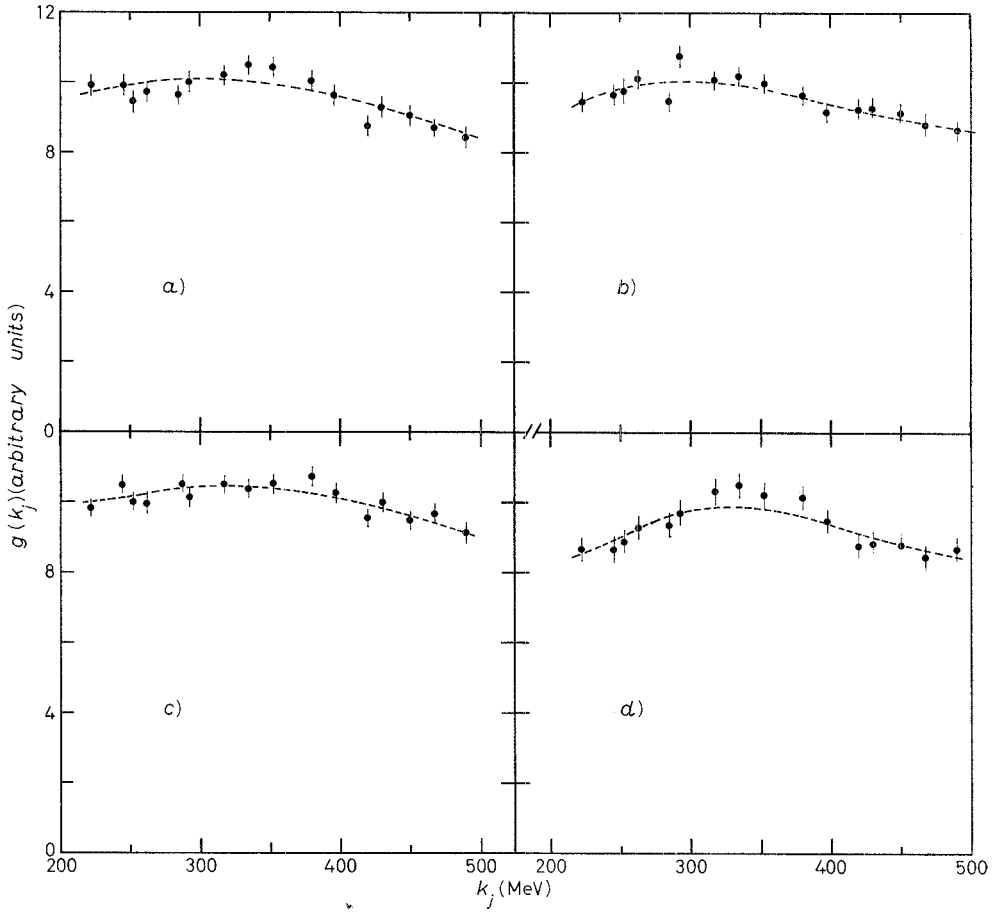

Fig. 6. – Photofission yields per equivalent quantum of Bi, Pb, Au and Pt as a function of the first peak energy k_j of photons. The dots are the experimental data; the dashed curves represent the yield functions estimated as described in sect. **5**. *a*) Bi (γ, f), *b*) Pb (γ, f), *c*) Au (γ, f), *d*) Pt (γ, f).

measured as described in subsect. **2**'1. We averaged the counts of the two glass plates of each sandwich in such a way to obtain results approximately free from a dependence on the forward/backward ratio, which, for the elements under investigation, resulted larger than 1 at all the k_j values. This ratio does not show apparently any dependence on the k_j energy within the experimental errors.

The obtained $g(k_j)$ values are given by the dots in fig. 6 and collected in table II as a function of the k_j energy; our data are in arbitrary units because we used thick targets.

TABLE II. – *Experimental yields* $g(k_j)$ *of* Bi, Pb, Au *and* Pt *as a function of the first peak energy* k_j *of photons.*

k_j (MeV)	$g(k_j)$ (arbitrary units)			
	Bi	Pb	Au	Pt
223	9.91 ± 0.30	9.44 ± 0.25	9.85 ± 0.25	8.68 ± 0.35
246	9.91 ± 0.30	9.65 ± 0.25	10.49 ± 0.26	8.63 ± 0.33
253	9.42 ± 0.28	9.80 ± 0.35	10.00 ± 0.25	8.92 ± 0.33
263	9.71 ± 0.28	10.17 ± 0.26	9.96 ± 0.25	9.27 ± 0.37
284	9.63 ± 0.27	9.50 ± 0.26	10.50 ± 0.25	9.35 ± 0.37
292	10.02 ± 0.29	10.79 ± 0.28	10.17 ± 0.26	9.76 ± 0.36
318	10.27 ± 0.31	10.10 ± 0.27	10.52 ± 0.26	10.35 ± 0.38
334	10.50 ± 0.31	10.19 ± 0.27	10.38 ± 0.26	10.50 ± 0.38
353	10.45 ± 0.31	9.92 ± 0.26	10.50 ± 0.26	10.22 ± 0.37
379	10.04 ± 0.30	9.65 ± 0.25	10.73 ± 0.26	10.14 ± 0.37
398	9.62 ± 0.28	9.13 ± 0.24	10.23 ± 0.26	9.48 ± 0.35
419	8.75 ± 0.30	9.27 ± 0.25	9.54 ± 0.25	8.73 ± 0.34
428	9.32 ± 0.27	9.30 ± 0.26	10.00 ± 0.26	8.81 ± 0.35
449	9.09 ± 0.26	9.16 ± 0.25	9.47 ± 0.25	8.78 ± 0.35
467	8.76 ± 0.25	8.81 ± 0.24	9.70 ± 0.26	8.41 ± 0.33
491	8.44 ± 0.30	8.64 ± 0.24	9.09 ± 0.25	8.70 ± 0.34

The bars in fig. 6 represent the accidental errors which have been calculated by taking into account i) the statistical error, ii) the reproducibility and the sampling errors of the scanning method, estimated as described in subsect. **2**'2.

The background contribution, due to spurious events in the glass plate itself, were estimated by scanning the surfaces of the plates not in contact with the target; it resulted to be negligible.

4. – Solution method of the integral equation of the process.

In our case, the equation connecting the fission cross-section $f(k)$ with the yields $g(k_j)$ is the linear Fredholm equation of the first kind

$$g(k_j) = \int_{E_t}^{E_0} \mathcal{N}(k, k_j) f(k)\, \mathrm{d}k \,. \tag{4}$$

where $\mathcal{N}(k, k_j)$ is the photon density per equivalent quantum as defined by eq. (3), E_t is a suitable energy at which the product $\mathcal{N}(k, k_j)f(k)$ is negligible with respect to its average value; we will call it for short « threshold energy ».

The solution method is described in detail in ref. ([32]). We will give here only the main features.

We discretized eq. (4) by a set of symoultaneous linear equations, because, contrary to YAMAGUCHI *et al.* ([27]), we preferred to avoid a best fit of the yields $g(k_j)$. In effect, small distortions in the yields may produce large non-physical oscillations in the solution ([22]), because, due to its mathematical structure, eq. (4) is essentially « unstable ». Thus we have the following system:

$$\sum_{i=1}^{N} a_{ji} f_i = g_j = g_j^* - \varepsilon_j \,, \qquad j = 1, \ldots, M \,, \tag{5}$$

or, in matrix form,

$$\boldsymbol{A}\boldsymbol{f} = \boldsymbol{g} = \boldsymbol{g}^* - \boldsymbol{\varepsilon} \,, \tag{6}$$

where

$A = \{a_{ji}\}$ is a matrix of $M \times N$ elements,

$\boldsymbol{f} = \{f_i\}$ is a column vector of N elements,

$\boldsymbol{g} = \{g_j\}$ is a column vector representing the « true » yields,

$\boldsymbol{g}^* = \{g_j^*\}$ is a column vector representing the experimental yields,

$\boldsymbol{\varepsilon} = \{\varepsilon_j\}$ is a column vector representing the unknown experimental errors.

We assume ε_j to be normally distributed with zero average, known variance σ_j^2 and zero covariance. From here on, we shall call V the variance-covariance diagonal matrix with diagonal elements σ_j^2. The last three vectors have M elements.

The elements of the A-matrix depend on the way the solution is represented. In other works the solution has been represented by step functions ([22]) or piecewise linear continuous functions ([24]). In order to improve the accuracy of the representation, the solution is approximated by a natural spline func-

tion ([35,36])

$$S(k) = \sum_{i=1}^{N} f_i \beta_i(u) , \tag{7}$$

where f_i are here placed at equally spaced values of k, and $\beta_i(u)$ are the cardinal splines ([35]) of the variable u defined as

$$u = (N-1)\frac{k - E_t}{E_0 - E_t} + 1 . \tag{8}$$

Thus the elements of the A-matrix are given by

$$a_{ji} = \int_{E_t}^{E_0} \mathcal{N}(k, k_j)\, \beta_i(u)\, \mathrm{d}k . \tag{9}$$

As far as the solution of eq. (6) is concerned, one can notice at once that the number of the equations is M, whilst the N quantities f_i and the M errors ε_j are unknown. Then we have a typical « ill-posed » problem that has the same characteristic of the starting problem. For this reason, it is necessary to introduce some auxiliary conditions to make our problem determined, without introducing a too large distortion in the solution.

Usually, the auxiliary conditions, imposed for the regularization of the solution, consist in the minimization of the curvature ([20]) and in the minimization of the departure from a trial solution, compatibly with an allowed value of the root-mean-square deviation between the experimental yields and those recalculated from the found solution ([21]). For a general account of the problem see ref. ([25]).

By using the technique of the Lagrange indetermined multipliers, our method consists in the search of the absolute minimum, with respect to $\boldsymbol{f}$, of the quadratic form

$$Q = p_1 \boldsymbol{f}^T C \boldsymbol{f} + p_2 (\boldsymbol{f} - \boldsymbol{t})^T W (\boldsymbol{f} - \boldsymbol{t}) + \gamma^{-1} (\boldsymbol{g}^* - A\boldsymbol{f})^T V^{-1} (\boldsymbol{g}^* - A\boldsymbol{f}) = \tag{10}$$
$$= Q_1 + Q_2 + Q_3 ,$$

where the first term (Q_1) represents the curvature, the second term (Q_2) the deviation from a trial solution and the third one (Q_3) the chi-square, which,

([35]) T. N. E. GREVILLE: in *Mathematical Methods for Digital Computers*, edited by A. RALSTON and H. S. WILF (New York, N.Y., 1967), vol. **2**, p. 156.
([36]) A. SARD and S. WEINTRAUB: *A Book of Splines* (New York, N.Y., 1971).

by taking into account eq. (6), is given by

$$\chi^2 = \sum_{j=1}^{M} \frac{\varepsilon_j^2}{\sigma_j^2} = \boldsymbol{\varepsilon}^T V^{-1} \boldsymbol{\varepsilon} \,. \tag{11}$$

In eqs. (10), (11) and in the following, T indicates the transposition operation. In eq. (10), p_1 and p_2 are two proper weights whose effects will be put in evidence later on; γ is the Lagrange multiplier, $\boldsymbol{t}$ is an assigned vector (trial solution), W is a diagonal matrix to be determined.

The errors ε_j being normally distributed, expression (11) is a statistics that has the chi-square distribution. The structure matrix C, defined in ref. ([21,32]), depends on the number of points N of the calculated solution and on the order of the derivative whose norm is required to be least. For our purposes it will be enough to have the solution with a small curvature, and for this we will use a derivative of order 2.

With the above conditions, the solution $\hat{\boldsymbol{f}}$ is estimated by the equation

$$\hat{\boldsymbol{f}} = [A^T V^{-1} A + \gamma(p_1 C + p_2 W)]^{-1} A^T V^{-1} \boldsymbol{g}^* + (I - R)\, \boldsymbol{t} \,, \tag{12}$$

where I is the identity matrix and

$$R = [A^T V^{-1} A + \gamma(p_1 C + p_2 W)]^{-1} A^T V^{-1} A \,. \tag{13}$$

If the matrix W is the identity, we go back to the combination of the methods proposed by PHILLIPS ([20]) and TWOMEY ([21]). With our kernel $\mathcal{N}(k, k_j)$ we verified that the first method alone is not sufficient to obtain a physically acceptable solution. On the other hand, the second one is unsuitable because we do not think to be convenient to assume information from the past history of the solutions ([1-16]) of different authors which are often in disagreement.

In order to eliminate all possible bias due to the imposition of a trial solution, we used the following procedure. By making an average on the Gaussian distribution of each error ε_j in eqs. (6) and (12), we find

$$A\boldsymbol{f} = \boldsymbol{g} = \bar{\boldsymbol{g}}^* \,, \tag{14}$$

$$\bar{\hat{\boldsymbol{f}}} = R\boldsymbol{f} + (I - R)\, \boldsymbol{t} \,, \tag{15}$$

where the bar indicates the average operation.

We notice that each element of the vector $\bar{\hat{\boldsymbol{f}}}$ is obtained by making the average on a very large number of experiments. If now the two conditions

$$\begin{cases} t_i = \text{constant} \,, \\ \sum_{l=1}^{N} R_{il} = 1 \,, \end{cases} \qquad i = 1, \ldots, N \,, \tag{16}$$

are satisfied, in eqs. (12) and (15) the term $(I - R)\,\boldsymbol{t}$ is identically zero. It is always possible to satisfy the second of the conditions (16) by an iterative process starting, for instance, from all equal elements of the diagonal matrix W, as shown in ref. ([32]).

When the conditions (16) are satisfied, eq. (15) becomes

$$\bar{\boldsymbol{f}} = R\boldsymbol{f}. \tag{17}$$

In this case, R is an operator that averages in energy the true solution and transforms it into the average of the estimated solution made on a very large number of experiments. Equations (16) and (17) suggest to interpret R as the energy resolution function, as shown by COOK ([22]). For instance, if $R_{il} = \delta_{il}$ (Kronecker symbol), one obtains $\bar{\boldsymbol{f}} = \boldsymbol{f}$. In this case the true $\boldsymbol{f}$ is not averaged in energy. Actually, the regularization process of the solution by the γ-parameter will give to the rows of the R matrix the typical bell shape of an energy resolution, and the second of conditions (16) will represent the normalization condition. Later on, we shall give some numerical example. When eqs. (16) are satisfied, eqs. (12) and (15) will be independent from $\boldsymbol{t}$. Therefore, for the sake of simplicity, we assume in eq. (10) all elements of the $\boldsymbol{t}$-vector vanishing; then our problem is reduced to estimating $\boldsymbol{f}$ and W in such a way that the quadratic form

$$p_1 \boldsymbol{f}^T C \boldsymbol{f} + p_2 \boldsymbol{f}^T W \boldsymbol{f} \tag{18}$$

will be least under the conditions

$$\begin{cases} \chi^2 = \text{constant}\,, \\ \sum_{l=1}^{N} R_{il} = 1\,, \end{cases} \qquad i = 1, \ldots, N\,. \tag{19}$$

5. – Photofission cross-section results.

By applying the unfolding method described in sect. 4 to the experimental yields, we obtained the cross-sections represented in fig. 7 and 8. We calculated the solution $\hat{\boldsymbol{f}}$ at equally spaced values of k, as required by the representation given by eq. (7). We chose the number of points $N = 16$, namely equal to the number of yields M, although this is not strictly necessary. Since the photofission cross-section for the elements we studied is negligible below 100 MeV, the solution $\hat{\boldsymbol{f}}$ was estimated at 16 points spaced 60 MeV from 100 to 1000 MeV, which is the maximum photon energy.

The errors, which are represented by the vertical bars in fig. 7 and 8, were calculated by means of the usual propagation rule. As these errors also account for the auxiliary conditions imposed to the solution, they do not

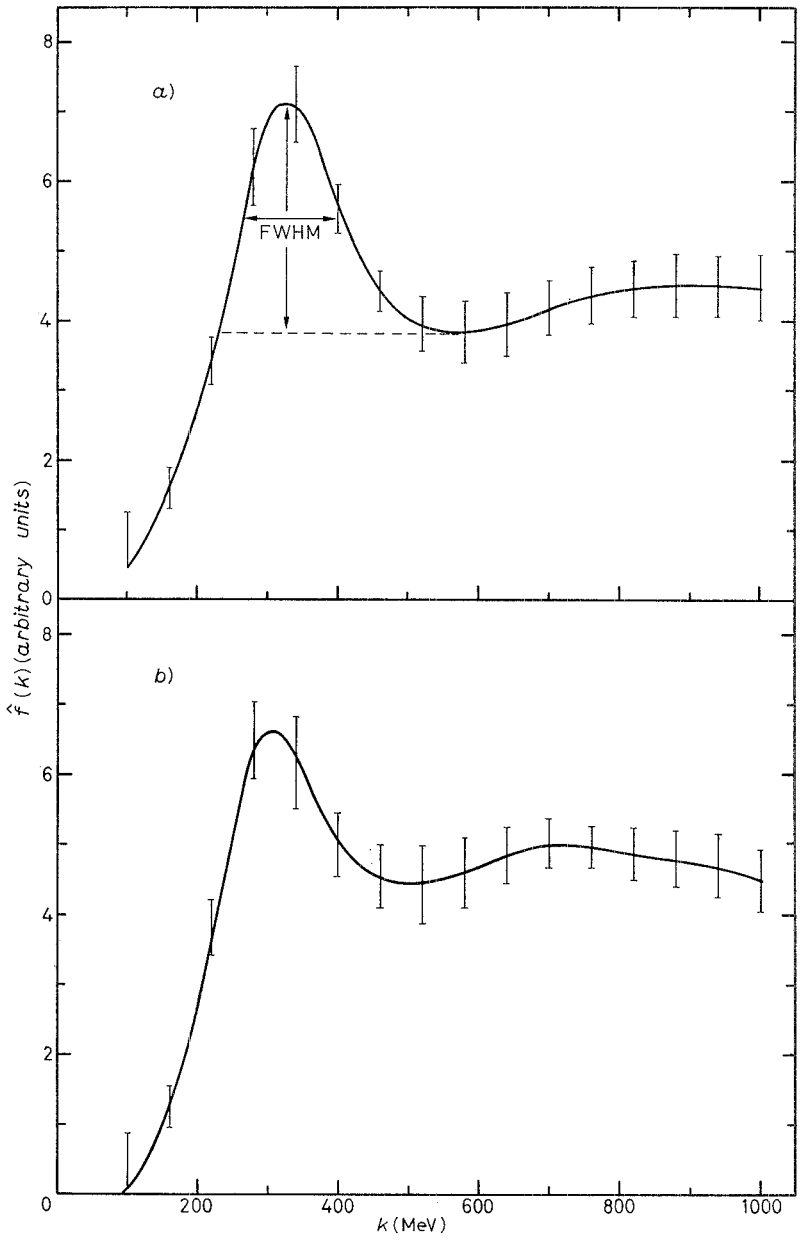

Fig. 7. – Photofission cross-section estimated by our unfolding method. For Bi the procedure used to deduce the FWHM of the first maximum is indicated. *a*) Bi (γ, f), *b*) Pb (γ, f).

represent the errors propagated only by the experimental ones. High values of the regularization parameter γ strongly constrain the solution; the length of the vertical bars in fig. 7 and 8 actually shows how much the solution is free. The $\hat{f}_i$ values and the corresponding errors, expressed in arbitrary units, are collected in table III.

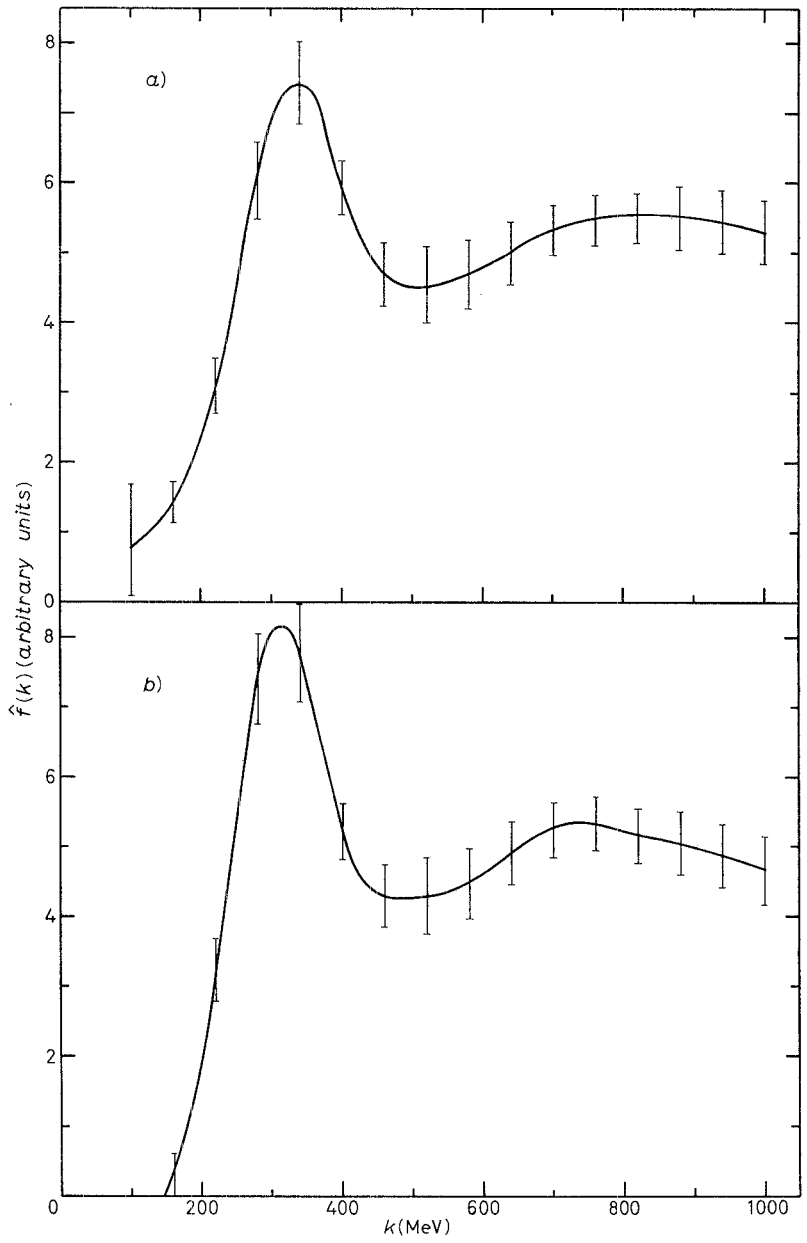

Fig. 8. – See caption to fig. 7. *a*) Au (γ, f), *b*) Pt (γ, f).

TABLE III. – *Estimated $\hat{f}_i$ values and corresponding errors.* All the data are given in arbitrary units.

k (MeV)	$\hat{f}(k)$ (arbitrary units)			
	Bi	Pb	Au	Pt
100	0.44 ± 0.80	0.07 ± 0.82	0.84 ± 0.81	-0.99 ± 0.88
160	1.63 ± 0.30	1.26 ± 0.32	1.42 ± 0.30	0.27 ± 0.37
220	3.43 ± 0.35	3.82 ± 0.43	3.11 ± 0.40	3.19 ± 0.45
280	6.20 ± 0.56	6.47 ± 0.55	6.02 ± 0.55	7.42 ± 0.67
340	7.12 ± 0.54	6.16 ± 0.64	7.43 ± 0.61	7.78 ± 0.64
400	5.61 ± 0.34	5.00 ± 0.46	5.93 ± 0.42	5.23 ± 0.40
460	4.42 ± 0.30	4.56 ± 0.47	4.70 ± 0.43	4.30 ± 0.46
520	3.94 ± 0.42	4.43 ± 0.58	4.54 ± 0.55	4.32 ± 0.55
580	3.83 ± 0.46	4.63 ± 0.50	4.70 ± 0.51	4.48 ± 0.51
640	3.95 ± 0.45	4.88 ± 0.42	5.01 ± 0.44	4.91 ± 0.45
700	4.18 ± 0.42	5.02 ± 0.35	5.33 ± 0.37	5.25 ± 0.40
760	4.35 ± 0.40	4.97 ± 0.33	5.47 ± 0.34	5.29 ± 0.39
820	4.44 ± 0.42	4.86 ± 0.36	5.50 ± 0.37	5.17 ± 0.41
880	4.49 ± 0.44	4.79 ± 0.40	5.47 ± 0.40	5.04 ± 0.45
940	4.50 ± 0.46	4.70 ± 0.43	5.45 ± 0.43	4.89 ± 0.47
1000	4.46 ± 0.47	4.50 ± 0.44	5.29 ± 0.45	4.67 ± 0.48

The solid curves in fig. 7 and 8 represent the $\hat{f}_i$ results interpolated by means of the spline functions (7).

All the relevant information of the estimated solutions is collected in table IV. Namely the regularization parameters γp_1 and γp_2, the contributions Q_1/Q, Q_2/Q and Q_3/Q of eq. (10) and the $\hat{\chi}^2$, as defined in eq. (11) and calculated by means of the $\hat{f}$, are given for each element under investigation. Moreover, the peak energy k_p and the full width at half maximum (FWHM)

TABLE IV. – *Values of the parameters characterizing the cross-section $\hat{f}$ curves plotted in fig. 7 and 8.*

Element	γp_1	γp_2	Q_1/Q	Q_2/Q	Q_3/Q	$\hat{\chi}^2$	k_p (MeV)	FWHM (MeV)
Bi	$27.0 \cdot 10^{-2}$	$6 \cdot 10^{-2}$	0.106	0.427	0.467	18.8	330	140
Pb	$8.4 \cdot 10^{-2}$	$6 \cdot 10^{-2}$	0.043	0.514	0.443	15.3	300	120
Au	$10.8 \cdot 10^{-2}$	$6 \cdot 10^{-2}$	0.060	0.557	0.383	14.1	340	120
Pt	$10.8 \cdot 10^{-2}$	$6 \cdot 10^{-2}$	0.131	0.534	0.335	12.5	315	120

are given for the first resonance. We calculated the FWHM by assuming the width relatively to the first minimum following the maximum, as shown in fig. 7 in the case of Bi.

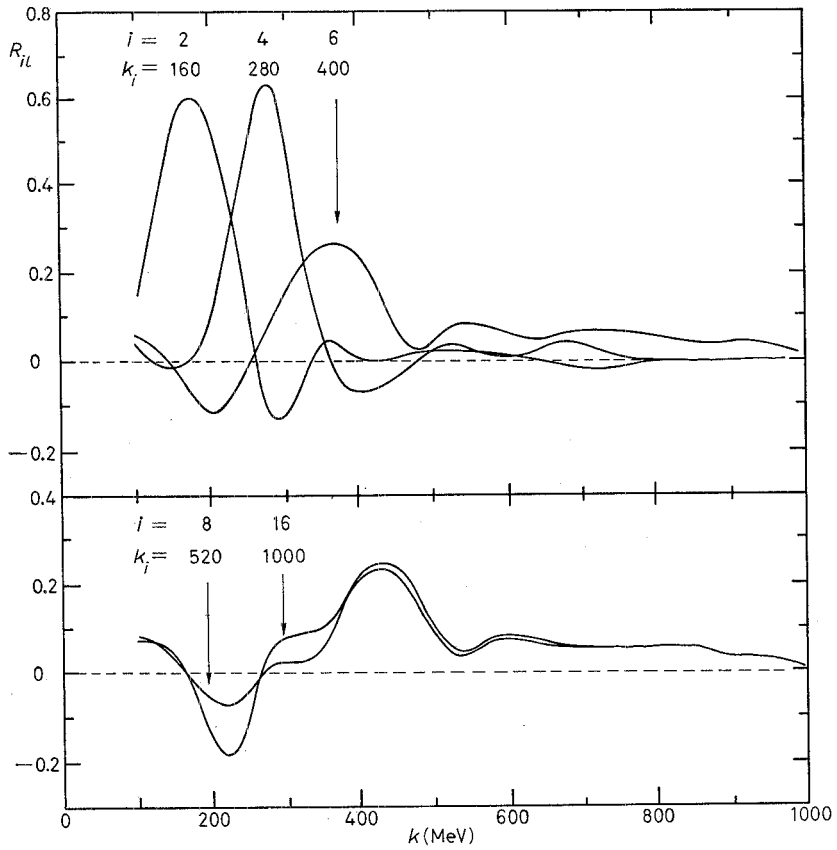

Fig. 9. – Elements R_{il} of the energy resolution matrix R obtained for Pt with the parameters collected in table IV.

Some elements R_{il} of the energy resolution matrix R are plotted in fig. 9 in the case of Pt. We obtained them at the parameter values of table IV. The solid curves were obtained by fixing the row index and by interpolating the 16 elements of each row by means of cubic spline functions. Owing to the normalization condition given by the latter of eqs. (19), the area delimited by each curve is equal to 1, as required for every resolution function. Thus, the imposition of this normalization condition, which is the central point of our method, appears to be completely natural. The effects of this condition on the W-matrix elements are discussed in detail in ref. ([32]).

Our preliminary results on Au reported in ref. ([17]) were obtained without fulfilling the latter of conditions (16). Therefore, the points above 500 MeV were practically bound to the values of the trial solution, and the photofission cross-section values were underestimated for $k < 500$ MeV and over-estimated for $k > 500$ MeV. As far as the other nuclides are concerned, the obtained curves for the R_{il} elements have essentially the same form.

The R-matrix rows plotted in the upper region of fig. 9 actually have the suitable form of an energy resolution function, apart from some small physically meaningless undershoot, with the maximum about in the correct position. When we look at the curves in the lower region of the same figure, it is clear that the experiment does not provide any reliable information above 500 MeV. Thus the cross-section behaviours of fig. 7 and 8 are much more reliable at energies below 500 MeV than above 500 MeV.

The criteria that guided us in selecting the γp_1 and γp_2 parameter values will be stated soon. We imposed $p_1 = 0$ in eq. (10) and, by minimizing the respective Q, we obtained some estimated solutions, which are indeed rather like those of fig. 7 and 8, apart from a few further oscillations. We chose the least value of γp_1, which is just enough to eliminate these oscillations, in such a way that also the Q_1 contribution in eq. (10) is small enough. Table IV shows that the maximum contribution of this correction expressed by the Q_1/Q term is 13 %. It is of interest to notice that we were able to obtain this result by using the same γp_2 value for all the investigated elements. We tried also to increase the smoothing parameter γp_1 without eliminating the first maximum in the cross-sections.

The $\hat{g}_i$ yields, recalculated from the $\hat{f}_i$ values, are shown in fig. 6 (dashed curves), compared with the experimental ones. The respective $\hat{\chi}^2$ values vary in a rather wide range with an average value $\bar{\hat{\chi}}^2$ equal to 15.2.

In order to estimate the γ-parameter, TURCHIN *et al.* ([25]) suggested a Bayesian method based on selecting an *a priori* statistical distribution of the solution. As this distribution is unknown, the choice always contains an element of arbitrariness and can be justified only by the successful utilization of the method itself. We tried to apply the method suggested in ref. ([25]), but we did not obtain any meaningful result.

6. – Discussion and conclusion.

The hatched area drawn in fig. 10 represents the region where the $\hat{f}_i$ values of all the four elements are contained. These values are normalized, so that their energy average from 100 to 1000 MeV is equal for all the elements. The area reproduces approximately the region of the errors of each curve of fig. 7 and 8. We can conclude that the cross-section behaviour is the same within

the experimental errors for the elements we studied; moreover, it is ascertained that the photofission cross-section shows a resonance at a photon energy of about 320 MeV with a mean FWHM $\approx$ 125 MeV (see table IV), whereas there is only a hint of a second very flat resonance centred at $k \approx 750$ MeV.

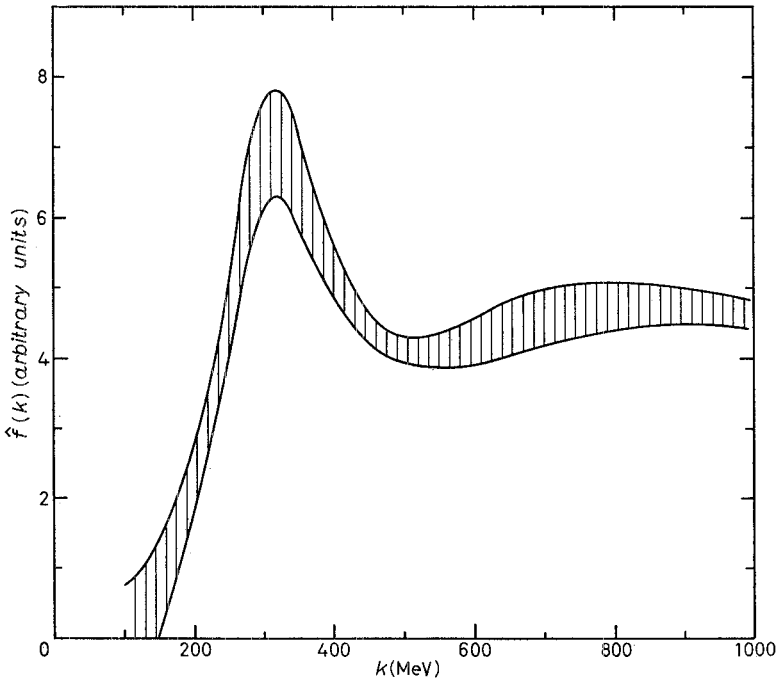

Fig. 10. – Region where the estimated $\hat{f}_i$ values of the elements we studied are contained.

Previously ANDERSSON *et al.* [15] had reported some cross-section curves which indicated the existence of a resonance for Pb and Au. These results, obtained by a bremsstrahlung beam from an « amorphous » target, show a rather broad peak around 400 or 500 MeV. For Au again and also for Bi, VARTAPETYAN *et al.* [14] had suggested cross-sections showing two resonances. By means of a folding method, these authors showed only that the photofission yields calculated from a model of photomesonic production are not incompatible with the experimental ones. Instead we demonstrate, by means of an unfolding method, that our experimental results obtained by a coherent photon beam are consistent only with resonant cross-sections. This result enables us to assert that the pion photoproduction, through the excitation of the first baryon resonance, plays an important role in the photofission process, at least for the elements we investigated. We had also a hint of a second resonance

at higher energy, but it was not possible for us to gain more information by means of the available photon beam.

* * *

We wish to thank the Frascati electronsynchrotron staff for the co-operation in performing the exposures, the members of the Frascati Sezione Calcolatore for the computer calculations and Mrs. C. GAROZZO for the accurate scanning work.

● RIASSUNTO

Sono state misurate le rese di fotofissione di Bi, Pb, Au e Pt indotta da un fascio di fotoni coerenti ottenuti per frenamento di elettroni da 1000 MeV su un monocristallo di diamante. I frammenti di fissione sono stati rivelati mediante sandwich di vetro. Il fascio di fotoni coerenti adoperato è caratterizzato da un picco principale « quasi monocromatico » sovrapposto ad uno spettro continuo. L'esperimento è stato eseguito a sedici differenti energie del picco principale nell'intervallo energetico compreso tra 220 MeV e 500 MeV. Poichè la posizione del picco principale di fotoni dipende criticamente dall'orientazione del monocristallo, ogni spettro è stato misurato contemporaneamente all'esposizione dei campioni fissionabili. Tale misura è stata eseguita mediante uno spettrometro magnetico e un sistema di acquisizione automatica in tempo reale con un calcolatore in linea. Allo scopo di dedurre l'andamento della sezione d'urto di fotofissione dalle rese sperimentali è stato sviluppato un appropriato metodo di deconvoluzione. Le curve ottenute per la sezione d'urto mostrano chiaramente una prima risonanza ad energia di fotoni di circa 320 MeV con una FWHM $\approx$ 125 MeV, mentre vi è soltanto l'accenno di una seconda risonanza centrata ad un'energia di circa 750 MeV. Si mette in evidenza come l'uso di un fascio di fotoni coerenti, adoperato per la prima volta in misure di fotofissione, ed il particolare metodo di deconvoluzione sviluppato hanno consentito di dedurre l'andamento risonante della sezione d'urto di fotofissione con maggiore attendibilità rispetto ai risultati della letteratura ottenuti con fasci di fotoni da targhette amorfe. L'ottimo accordo tra l'energia della prima risonanza, messa in evidenza nel presente esperimento, e l'energia della prima risonanza barionica nella fotoproduzione di pioni è ritenuto un'indicazione del prevalere del meccanismo fotomesonico nel processo di fotofissione per gli elementi studiati.

Деление висмута, свинца, золота и платины, индуцированное когерентным фотонным пучком от 1000 МэВ электронов.

Резюме не получено.